

Cite this: *Mater. Adv.*, 2024,
5, 9018

Improved performance of a SWCNT/ZnO nanostructure-integrated silicon thin-film solar cell: role of annealing temperature

Nandang Mufti,^{id}*^{ab} Olga Dilivia Ardilla,^a Erma Surya Yuliana,^a
Retno Fitri Wulandari,^a Ahmad Taufiq,^{id}^{ab} Henry Setiyanto,^{id}^c
Muhammad Aziz,^{id}^d Ali Aqeel Salim,^{be} Risa Suryana^f and Wilman Septina^g

Efficiency improvement of heterogeneous silicon thin-film solar cells (SiTFSCs) remains challenging. Thus, single-walled carbon nanotube (SWCNT) and zinc oxide nanostructures (ZnO NCs) were integrated into Si thin films using the spray-spin coating approach to realize such solar cells. The effect of various annealing temperatures (100–175 °C) on the solar cells' efficiency, structure, morphology, and absorbance was assessed. X-ray diffraction analysis confirmed the existence of highly crystalline wurtzite and hexagonal structures corresponding to ZnO and graphite with maximum nanocrystallite sizes of 51.92 nm. Scanning electron microscopy images of the samples showed uniform surface morphology without any aggregation. In addition, with the increase of the annealing temperature from 100 to 175 °C, the efficiency, porosity, optical absorbance bands, and band gap energy of the films were increased from 17.0–18.6%, 70–74.8%, 246–326 nm, and 2.0–2.5 eV, respectively. It was asserted that by controlling the annealing temperature, the overall performance of the proposed SWCNT/ZnO NC-integrated SiTFSC can be enhanced, contributing to the further advancement of high-performance Si-based photovoltaics.

Received 18th July 2024,
Accepted 17th October 2024

DOI: 10.1039/d4ma00726c

rsc.li/materials-advances

1. Introduction

Global energy consumption has rapidly increased in recent years, particularly the demand for electrical energy.^{1,2} The reliance on fossil fuels for power generation is one of the most pressing environmental challenges and is inadequate to fulfill this escalating demand for electricity.² In contrast, solar energy is an abundant, clean, and renewable resource that offers an environmentally sustainable alternative.³ Photovoltaic cells are designed to convert light energy into electricity using semiconductor materials.⁴ These materials facilitate the flow of

electrons when they absorb photons from sunlight, causing the ejection of electrons and creating vacancies in the material.^{5,6} The photovoltaic effect is the phenomenon whereby the absorption of photons leads to the generation of electron flow.^{1,7} Recently, the development of carbon-based materials has gained considerable attention due to their abundant natural availability.^{8,9} The unique crystalline structure and electrical characteristics of these materials, which exhibit both sp² and sp³ hybridization, enable carbon to bond with silicon forming carbon–silicon (C/Si) heterojunctions.⁹ Heterojunction devices incorporating thin films of carbon nanotubes (CNTs), graphene, and polymers have revealed rapid development as innovative solar cell technologies.^{8–10} These materials provide several advantages, including significant improvements in the efficiency and performance of the fabricated solar cells.^{9–11}

Silicon-based solar cells dominate approximately 97% of the global market due to the superior efficiency and long-term stability of p–n junction silicon solar cell technology.¹¹ Besides, silicon is the most widespread material used in solar cells with a band gap of 1.12 eV.¹² Nonetheless, the high production costs and complex fabrication processes associated with silicon solar cells present considerable challenges to their widespread usage.¹³ In contrast, emerging materials such as carbon nano-materials offer promising alternatives that could enhance both

^a Department of Physics, Faculty of Mathematics and Natural Sciences, Universitas Negeri Malang, Jl. Semarang 5, Malang, 65145, Indonesia.
E-mail: nandang.mufti.fmipa@um.ac.id

^b Center of Advanced Materials for Renewable Energy, Universitas Negeri Malang, Jl. Semarang 5, Malang, 65145, Indonesia

^c Analytical Chemistry Research Group, Institut Teknologi Bandung, Jl. Ganesha 10 Bandung, 40132 Bandung, Indonesia

^d Institute of Industrial Science, The University of Tokyo, Tokyo, Japan

^e Laser Centre, Ibnu Sina Institute for Scientific and Industrial Research, Universiti Teknologi Malaysia (UTM), 81310 Skudai, Johor D.T., Malaysia

^f Department of Physics, Faculty of Mathematics and Natural Sciences, Universitas Sebelas Maret, Surakarta 57126, Indonesia

^g Research Center for Electronics, National Research and Innovation Agency (BRIN), Bandung, Indonesia



the efficiency and stability of solar cell technologies with a reduction in production costs.¹⁴ Furthermore, it possesses advantageous attributes such as flexibility, extensive surface area, high carrier mobility, stability, and exceptional optoelectronic properties, which are well-suited to the demands of heterojunction applications.^{14–16} Currently, carbon nanotubes (CNTs) are being actively developed within the solar cell industry.¹⁵ CNTs can be conceptualized as hollow cylinders formed by rolled graphene-bonded pure carbon.¹⁷ This distinctive structure endows CNTs with excellent electron mobility, an optimal band gap, superior optical properties, robust stability, high conductivity, and transparency.^{18–20} Moreover, single-walled carbon nanotubes (SWCNTs) are a type of p-type semiconductor with higher efficiency due to their high transparency and low resistivity.^{18,20} The purity of SWCNTs is critical for maintaining optimal performance due to the as-synthesized SWCNTs still retaining various impurities, such as metal catalysts, amorphous carbon, and residual catalyst particles. These contaminants can adversely affect the structural and electrical properties, leading to a decline in performance.^{21,22} Consequently, SWCNT purification and functionalization are important to improve their quality and ensure their effectiveness in advanced applications.

Various physical and chemical methods have been used to synthesize SWCNT nanostructure materials, including chemical vapor deposition (CVD), sol-gel processes, and atomic layer deposition (ALD).^{23–27} These techniques offer superior control over the size, morphology and uniformity of the nanostructures (NCs), which is crucial for optimizing their integration into advanced solar cell technologies.^{23,24} To improve the overall performance of integrated solar cell systems, it is particularly important to produce high-purity SWCNTs and ZnO NCs with fewer defects in their physical structure. On top, one of the most effective and commonly used methods for the high-purity and functionalization of SWCNTs is chemical purification *via* acid treatment, particularly with hydrochloric acid (HCl).²⁸ It is favored due to its simplicity and efficiency in removing impurities such as metal catalysts. Acid purification has proven to be highly effective in significantly reducing metal contamination in SWCNTs.²⁸ However, the choice of acid is dictated by the balance between purity levels and CNT preservation.²⁹ SWCNT/ZnO nanostructures possess unique physical properties including exceptional electron mobility, high surface area, and strong optoelectronic characteristics.^{18,30} SWCNTs are known for their flexibility, transparency, and superior electrical conductivity,³⁰ while ZnO nanostructures provide excellent UV absorption and a wide bandgap, making them ideal for photovoltaic applications.^{31,32} ZnO is a widely utilized semiconductor material due to its excellent thermal stability, superior performance with a bandgap ranging from 3.1 to 3.3 eV, and high electron mobility of $1000 \text{ cm}^2 \text{ V}^{-1} \text{ s}^{-1}$.^{33–35} Wang *et al.* demonstrated that the integration of a ZnO coating in SWCNT/Si solar cells significantly enhanced their efficiency from 1.3% to 4.0%.³⁶ These improvements emphasize the potential of ZnO as a critical material for optimizing the performance of next-

generation solar cells.^{36,37} Gurova *et al.*²⁰ reported that the purification of SWCNTs was achieved using HCl, HNO₃, H₂SO₄, and a HNO₃/H₂SO₄ (3:1) mixture, resulting in a relatively high purity of 97–99%. Furthermore, hydrochloric acid treatment is highly effective and does not damage the surface structure.²⁰ In contrast, treatment with the HNO₃/H₂SO₄ mixture induces considerable oxidation, leading to surface deterioration.³⁸ These SWCNT/ZnO NCs synergistically improve charge separation and reduce recombination rates, making silicon thin-film solar cells more efficient.³⁹

The integrated cells demonstrate a significant improvement in light absorption, electron transport, and conversion efficiency compared to traditional silicon cells and other nanomaterial combinations such as TiO₂, MoS₂, SiO₂, SOCl₂, and ZnO.^{17,21,40} Earlier, several studies observed that the incorporation of TiO₂ into SWCNT/Si solar cells significantly enhanced their efficiency using the CVD method at 1160 °C, resulting in an efficiency of 15%.⁴¹ Moreover, Saidah *et al.* have reported an optimized CVD process conducted at 850 °C in a furnace, leading to further efficiency of 17%.²³ The innovation of this research lies in its comprehensive strategy to enhance solar cell performance by optimizing the coating process and thermal treatment.⁴² Thus, this research examined the influence of various annealing temperatures (ranging from 100 to 175 °C) on the surface morphology, optical, and electrical properties of SWCNT coatings prepared using the spray coating method. Furthermore, it assessed the overall efficiency of silicon solar cells coated with SWCNT/ZnO NCs. A purification process involving a combination of HCl, HNO₃, and H₂SO₄ was chosen due to its superior effectiveness in eliminating impurities, particularly iron. These SWCNT/ZnO NCs exhibit significant promise and could be a great candidate material as cost-effective, stable, and high-performance materials for photovoltaic applications.

2. Experimental procedures

2.1. Materials and layer deposition of SWCNT/ZnO NCs on a Si thin film

Various materials including SWCNTs (95% purity), Zn(CH₃COOH)₂·2H₂O, ethanol (C₂H₅OH, 99.5%), and monoethanolamine (MEA) were purchased from Merck. First, 0.5 g of SWCNTs were purified and functionalized in 100 mL of 37 wt% HCl, followed by 4 hours of sonication to ensure proper dispersion. The molar ratio of HCl and H₂SO₄ is determined to be 12 M. The solution was filtered and washed to achieve a neutral pH 7 and then dried at 100 °C for 12 hours. The process was repeated using 200 mL of H₂SO₄ and HNO₃ mixture in a 3:1 ratio. Once dried, 0.03 g of the powder was mixed with 100 mL of 3 wt% sodium dodecyl sulfate (SDS) for 48 hours and sonicated for 2 hours at a temperature of 13–15 °C. Finally, the mixture was centrifuged at 3600 rpm for 1 hour to separate the supernatant and precipitate, resulting in a stable SWCNT suspension. Subsequently, 1 mL of the SWCNT suspension was sprayed onto silicone and placed upon a hotplate set at





Fig. 1 Schematic illustration of the deposition mechanism for the SWCNT/ZnO NC integrated Si thin film.

100 °C. The residual solvent film was annealed at various temperatures of 100 °C, 125 °C, 150 °C, and 175 °C for 10 min to form Si/SWCNT films. Second, 0.88 g of $\text{Zn}(\text{CH}_3\text{COOH})_2 \cdot 2\text{H}_2\text{O}$ was combined with 20 mL of ethanol and agitated for 45 min at 90 °C. Thereafter, 0.24 L of MEA was added and stirred for an additional 60 min. The obtained ZnO solution was dripped onto the Si/SWCNT films and spun at 3000 rpm for 20 s after a 24-hour interval. Lastly, the Si/SWCNT/ZnO NC thin film was dried on a hotplate at 100 °C for 3 hours. A schematic of the SWCNT/ZnO NC deposition process on a Si substrate is illustrated in Fig. 1.

2.2. Characterizations of the SWCNT/ZnO NC deposition layers

The Si/SWCNT/ZnO films were characterized using X-ray diffraction (XRD), PANalytical, and X'Pert Pro, with monochromated Cu-K α 1540 Å to determine the diffraction patterns. The morphology and structural properties were determined by scanning electron microscope (SEM), FEI, and Inspect-S50. The absorbance spectra and energy band-gap were analyzed by using an ultraviolet-visible (UV-vis), Analytik Jena Specord 200 plus spectroscopy, and also *I-V* testing using a solar simulator (Model 10500) to determine the solar cell efficiency of Si/SWCNT/ZnO. In addition, current and voltage photodetectors were also measured. The samples were coded to represent their compositions and annealing temperature variations. The purified Si/SWCNT thin film was designated as P-SW, whereas the Si/SWCNT/ZnO thin films were labelled as P-SWZ-100, P-SWZ-125, P-SWZ-150, and P-SWZ-175, corresponding to annealing temperatures of 100 °C, 125 °C, 150 °C, and 175 °C, respectively.

3. Results and discussion

Fig. 2 shows the XRD patterns of SWCNT/ZnO NCs film obtained at various annealing temperatures. The XRD analysis revealed SWCNT diffraction peaks at 25.12° and 44.15° corresponding to the (002) and (100) planes, respectively. In addition, the most prominent peak was observed at 38.15°, attributed to the (111) diffraction of silicon.⁴³ The P-SW sample exhibited a 2θ peak at 25.12°, assigned to the (002) plane of the hexagonal graphite structure, which indicated the carbon reflection.⁴³ Besides, the diffraction pattern of the P-SWZ samples prepared at various annealing temperatures exhibited a slight shift of the



Fig. 2 Diffraction patterns of SWCNT and SWCNT/ZnO NC integrated Si thin film.

carbon peak from its original position at 25.12°. The P-SWZ-100, P-SWZ-150, and P-SWZ-175 samples revealed a very weak shift of the carbon peak from 25.12° to 28.33°, indicating changes in the carbon crystallinity and structural modifications in the SWCNTs.³⁹ This shift can be attributed to the interaction between SWCNTs and ZnO during the annealing process. Consequently, ZnO NCs can interact with SWCNTs through the formation of covalent bonds or *via* van der Waals forces.³⁹ The diffraction patterns of the P-SWZ samples clearly exhibited ZnO peaks at 64.50° and 77.37°, corresponding to the (103) and (202) planes, respectively. Furthermore, the absence of prominent ZnO peaks in the XRD patterns can be attributed to the thinness of the ZnO film, its lower crystallinity, and smaller volume relative to the SWCNT materials.^{39,44} All ZnO peaks demonstrate a wurtzite crystal structure with the space group $P63mc$, as reported in AMCSID no. 5203.⁴⁴ In addition, Rietica analysis provided the lattice parameters $a = b = 3.250$ Å and $c = 5.206$ Å. The crystallite size was determined using the Debye-Scherrer equation, as indicated in eqn (1).⁴³

$$D \text{ (nm)} = \frac{K\lambda}{\beta \cos \theta} \quad (1)$$

where $K = 0.9$; $\lambda = 1.5406$ Å, β is the value of full-width half





Fig. 3 SEM images of the P-SW sample: (a) top-view, (b) cross-section, and (c) diameter distribution curve.

maximum (FWHM), and θ is the diffraction peak angle.³¹ Our calculations determined a ZnO crystallite size of 51.92 nm, aligning with average crystallite sizes ranging from 12–85 nm reported by Mahesh *et al.*⁴⁵ Diffraction studies indicate that higher annealing temperatures result in more pronounced peaks. Specifically, the SWCNT peak at 44.15° showed a slight increase after the annealing process. This increase in diffraction intensity is attributed to the elevated annealing temperature, which leads to greater incorporation of silicon into the SWCNT matrix and strengthens the bonding between individual nanotubes, resulting in a higher degree of crystallinity. The measurement results indicate that the size of SWCNT in the P-SW sample was 1.26 nm, which is comparable to the early reported size of 0.91 nm.⁴⁶

Fig. 3 depicts the surface morphology and cross-sectional structure of the purified SWCNT thin films without the addition of ZnO, observed through SEM analysis at $20\,000\times$ magnification. Fig. 3(a and b) shows the SEM images of the P-SW sample coated on a silicon substrate along with the cross-sectional view of a $1.4\ \mu\text{m}$ thickness. Fig. 3(c) reveals the

diameter distribution curve of the P-SW sample with diameters ranging from 80–90 nm. These findings are consistent with the research work of Zuo *et al.*⁴⁷

Fig. 4 illustrates the surface morphology and cross-sectional structure of the purified SWCNT thin films with the addition of ZnO prepared at various annealing temperatures alongside corresponding size distribution curves. The SEM images reveal a uniform surface morphology across all variations with no significant agglomeration observed at higher annealing temperatures, as evidenced by the smaller average diameter of the SWCNT fibers. Tripathi *et al.*⁴⁸ noted that higher annealing temperatures yield smaller diameters and enhanced structural quality of the SWCNTs. The average diameter distribution of the SWCNTs for each temperature variation is listed in Table 1.

Fig. 5 presents the porosity analysis of SWCNT/ZnO NCs based on Si films across different annealing variations. The porosity of Si/SWCNT/ZnO NCs is primarily influenced by the pore area or vacant space, rather than the solid region. Porosity is characterized as the ratio of void volume to the total volume of the sample. An increase in porosity indicates that a larger

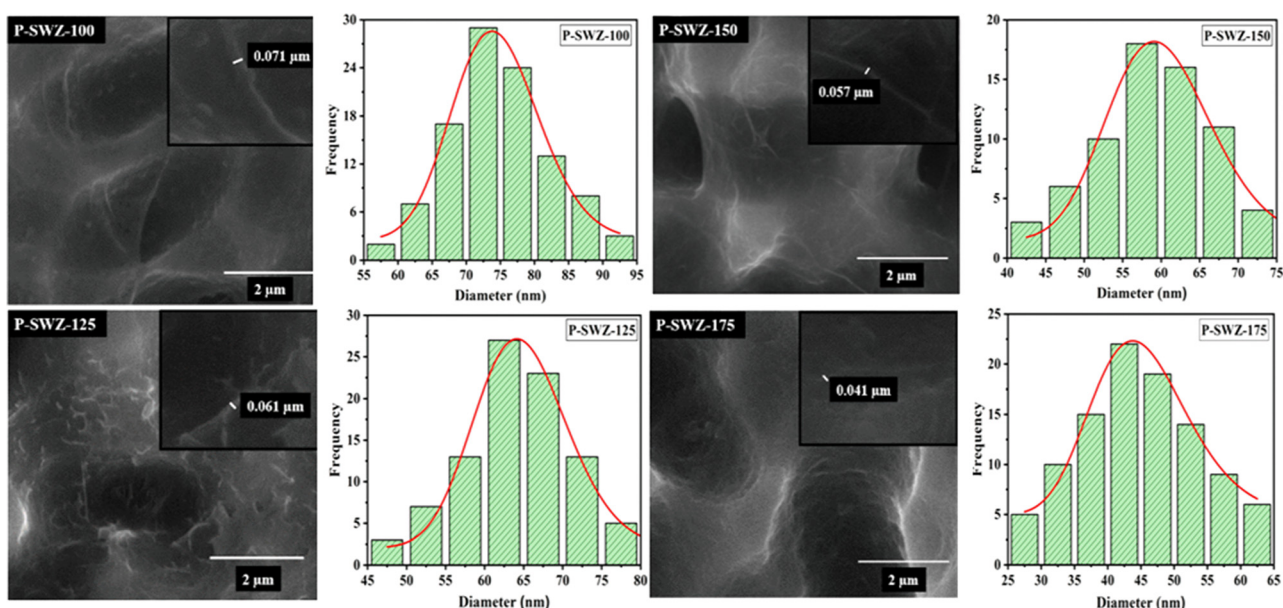


Fig. 4 SEM images of SWCNT/ZnO NC integrated Si thin films prepared at various annealing temperatures.



Table 1 Sample codes, surface structure, and optical properties of the SWCNT/ZnO NC-based Si thin film

Sample code	Temperature (°C)	Crystal size (nm)	Fiber diameter (nm)	Porosity (%)	E_g (eV)
P-SW	0	29.7	87 ± 1.2	63.9	2.00
P-SWZ-100	100	39.3	74 ± 0.3	70.0	2.55
P-SWZ-125	125	55.9	65 ± 0.5	73.0	2.53
P-SWZ-150	150	74.4	57 ± 0.6	73.2	2.51
P-SWZ-175	175	101.4	41 ± 0.6	74.8	2.50

portion of the sample remains unoccupied by the SWCNT/ZnO matrix. Enhanced porosity can be obtained due to the formation of voids during the synthesis process, the removal of solvents, and the arrangement of SWCNTs and ZnO particles that create larger interstitial spaces. Table 1 provides the porosity values for each annealing variation, demonstrating that higher annealing temperatures lead to increased porosity.

Furthermore, the increase in the porosity value is also associated with a smaller diameter size and a larger surface area. The percentage of porosity was obtained using an equation shown in eqn (2).

$$\text{Porosity (\%)} = \left(\frac{\text{Volume of voids}}{\text{Total volume}} \right) \times 100 \quad (2)$$

Fig. 6(a-d) exemplifies the SEM cross-sectional images of SWCNT/ZnO NC samples (labelled as P-SWZ-100, P-SWZ-125, P-SWZ-150, and P-SWZ-175) prepared at various annealing temperatures. The films exhibited consistent results across the temperature range with a thickness of ~1.5 μm. Despite uniform thickness, the cross-sectional images revealed irregularities in the SWCNT/ZnO NCs layer on the silicon surface. This phenomenon can be attributed to the differing deposition techniques used for SWCNT and ZnO. Variations in spray



Fig. 5 Porosity graphs of SWCNT/ZnO NC integrated Si substrates at various annealing temperatures.



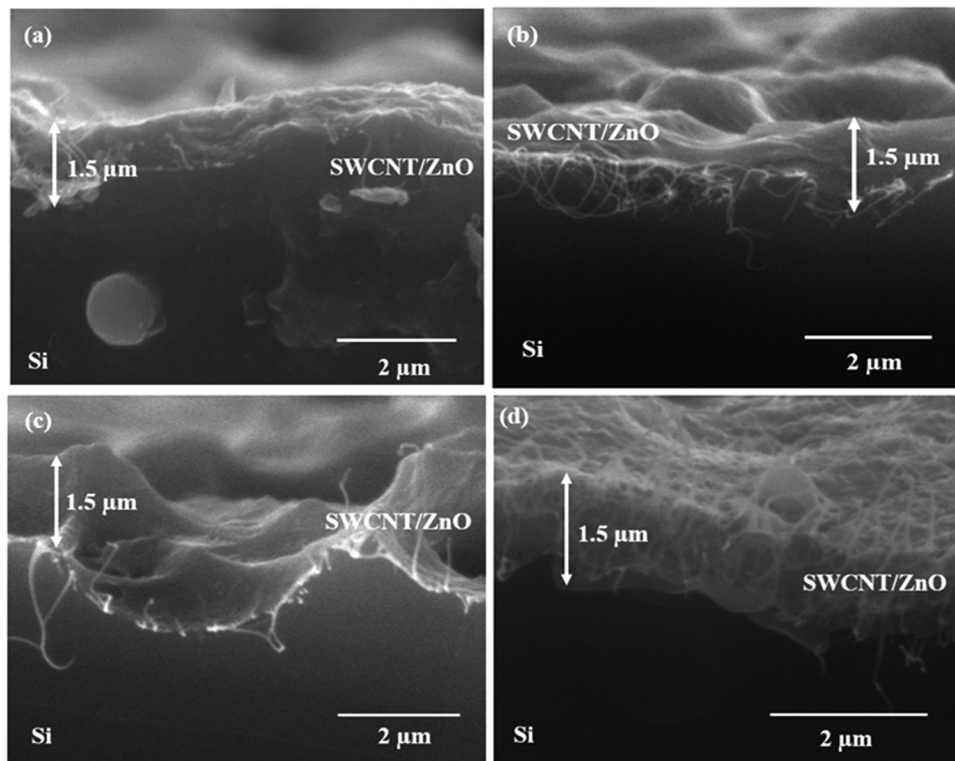


Fig. 6 SEM cross-section images of the SWCNT/ZnO NC based Si thin film prepared at various annealing temperatures: (a) 100 °C, (b) 125 °C, (c) 150 °C, and (d) 175 °C.

coater pressure and distance as well as the solution drip rate during spin coating of ZnO may significantly influence the final structure. Consequently, these variations can lead to alterations in the SEM cross-section of the SWCNT/ZnO NCs.

Fig. 7 shows the absorption spectra of the SWCNT/ZnO NC-based Si thin film prepared at various annealing temperatures with wavelength ranges of 200–1000 nm. The SPR absorbance peaks were observed in the wavelength range of 246–282 nm,

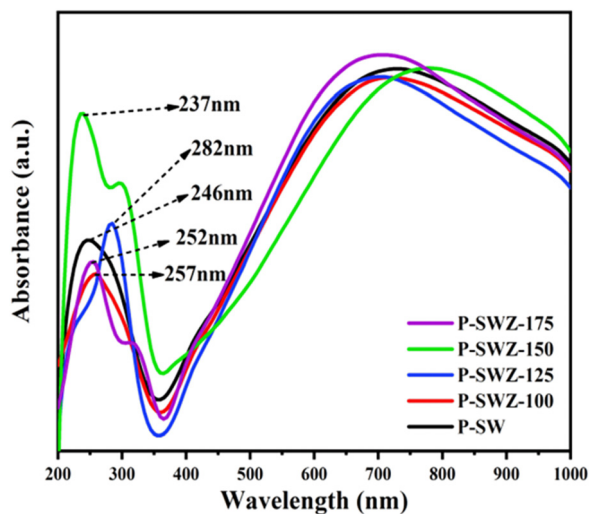


Fig. 7 UV-vis absorption spectra of the SWCNT and SWCNT/ZnO NC integrated Si thin film.

respectively. The wavelength of the P-SW and P-SWZ samples in the UV region exhibits a blue shift, indicating an increase in the electronic transition energy in ZnO. This increase may be attributed to the changes in the molecular structure of ZnO and stronger interactions between ZnO and SWCNT materials. In addition, the P-SWZ samples, across all variations, display absorbance bands in the 620 to 920 nm range which corresponded to the metallic and semiconducting transitions.⁴⁹ Higher temperatures lead to increased absorbance values, indicating that elevated annealing temperatures may accelerate the evaporation of oxygen during the annealing process. The high absorbance value also affected the amount of light being absorbed and passed through. The results from all samples showed absorbance values in the UV light range (< 400 nm).⁵⁰

Fig. 8 illustrates the linear fitting of E_g between SWCNT and SWCNT/ZnO NCs based on Si films. The E_g values at different annealing temperatures exhibit a slight decrease (Table 1). The P-SW sample produced an E_g of 2.00 eV, which is comparable to a previous study reporting $E_g = 1.75$ eV.⁵¹ The variation in values is attributed to the chemical treatment of the SWCNTs. In contrast, the P-SWZ sample displayed an E_g around 2.50 eV, which is higher than that of P-SW. This increase is due to the addition of ZnO, which has an intrinsic E_g of approximately 3.33 eV. Ziat *et al.* reported a reduction in E_g for SWCNT/ZnO NCs from 2.76 eV to 2.31 eV,⁵² aligning with the E_g values obtained in this study. A lower E_g is advantageous for enhancing photovoltaic efficiency. Variations in annealing temperature for P-SWZ samples resulted in different E_g values.





Fig. 8 Fitting energy band-gap of the SWCNT and SWCNT/ZnO NC integrated Si thin film.

Annealing at 100 °C produced an E_g of 2.55 eV, while the maximum E_g for P-SWCNT/ZnO NC-based Si films was achieved at 175 °C. The reduction in E_g leads to higher absorbance and a smaller energy gap between the conduction and valence bands, facilitating electron transfer and improving the device's conductivity.⁵³ To assess optoelectronic properties, SWCNT/

ZnO NCs on Si films were packaged for photodetector analysis. Photocurrent generation is influenced by electronegative O_2 molecules adsorbed on the ZnO surface, which desorb under light due to charge neutralization by holes, releasing free electrons. These free electrons then flow as photocurrent under an external bias. However, free electron instability may occur,



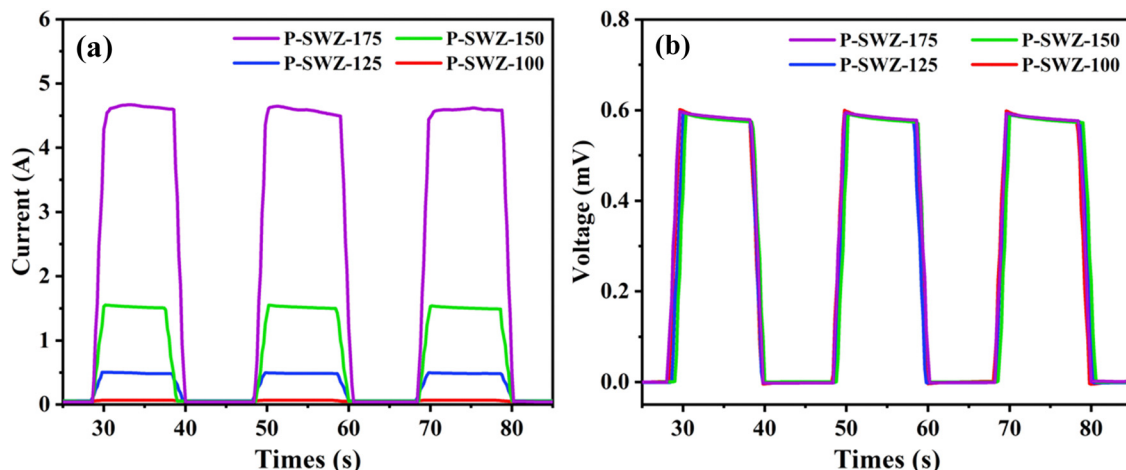


Fig. 9 The photodetector response of SWCNT/ZnO NCs: (a) current and (b) voltage.

with unpaired electrons being transferred to the SWCNTs, preventing electron-hole recombination and enhancing device performance.³⁵ Under light irradiation, photodetectors generate electron-hole pairs due to the photoelectric effect. Test results

indicate that higher light intensities produce greater photocurrent, as the increased number of photons generates more electron-hole pairs. Conversely, when light intensity decreases, electron-hole recombination increases, reducing the photocurrent.⁵⁴

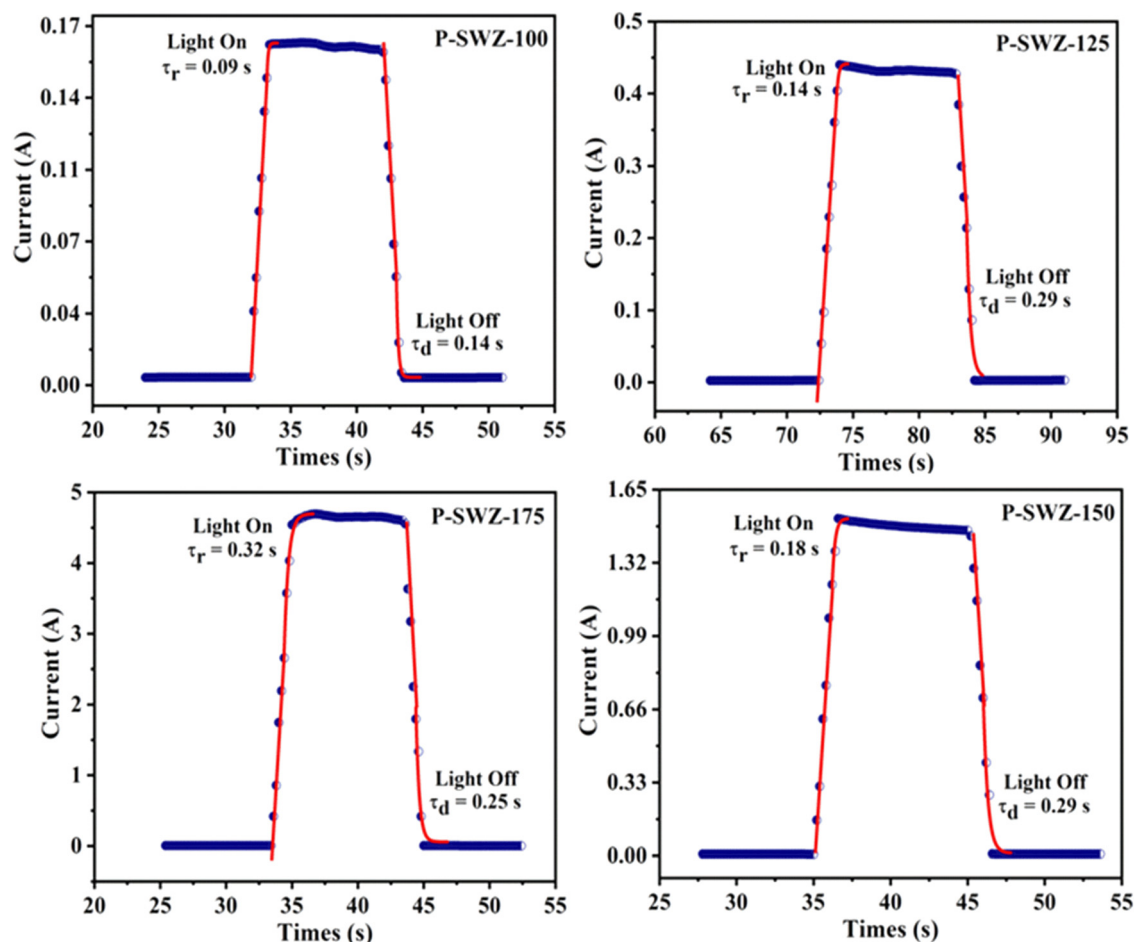


Fig. 10 Photoresponse current fitting of SWCNT/ZnO NCs on Si thin films.





Fig. 11 Photovoltage response fitting SWCNT/ZnO NCs on the Si thin film.

Fig. 9(a and b) depicts the photodetector response of the current and voltage as a function of time for SWCNT/ZnO based Si solar cell samples prepared at different annealing temperatures. The measurements were taken at alternating 10-second intervals under irradiated and non-irradiated light conditions using a solar simulator providing a constant light intensity of 100 mW cm^{-2} . The packaging process for the photodetector analysis of SWCNT/ZnO NCs on Si films was meticulously designed to ensure the device stability and functionality. The SWCNT/ZnO NC samples were uniformly deposited onto the Si films using the spin-coating technique. These samples were then subsequently annealed at different temperatures to improve the material adhesion and optimize the interface quality, allowing effective light penetration for optoelectronic testing. Consequently, the device exhibited a strong photocurrent response with a rapid increase in photocurrent under illumination. Conversely, the photocurrent dropped to zero under non-irradiated conditions, indicating electron-hole recombination.^{31,35} Higher annealing temperatures enhanced photocurrent due to improved free electron stability and more efficient pathways for photocarrier transport.

Fig. 10 and 11 show the fitting curves of the photodetector to the current and voltage responses. The device response carried

a vital parameter, namely the photodetection speed, consisting of rising time (τ_r) and decay time (τ_d).⁵⁴ It is found that the rise time of the P-SWZ device is shorter than the decay time due to an increase in electron transport. Table 2 demonstrates the current response, where the P-SWZ-100 produces a shorter response time than other devices, namely 0.09 s and 0.14 s. Additionally, the P-SWZ-175 presented a relatively large rise and decline time of 0.32 s and 0.25 s, respectively. The difference in time patterns between the two is due to the difference in wavelength, as confirmed by Walmsley *et al.*⁵⁵ Besides, the shorter wavelength produces higher photo carrier energy, so it has a high probability of overcoming the Schottky barrier on ZnO. Thus, the obtained response time is relatively fast, and *vice versa*. Choi *et al.*⁴⁴ used a light intensity of 0.47 mW cm^{-2} to measure the photocurrent response of the samples. The

Table 2 Photovoltage response of SWCNT/ZnO NCs on Si thin films

Sample	Rising time (τ_r) (s)	Decay time (τ_d) (s)
P-SWZ-100	0.09	0.14
P-SWZ-125	0.14	0.29
P-SWZ-150	0.18	0.29
P-SWZ-175	0.32	0.25



Table 3 Photoresponse voltage of SWCNT/ZnO NCs on the Si thin film

Sample	Rising time (τ_r) (s)	Decay time (τ_d) (s)
P-SWZ-100	0.05	0.14
P-SWZ-125	0.04	0.06
P-SWZ-150	0.04	0.04
P-SWZ-175	0.09	0.10

photocurrent as a function of time was analyzed for both bare ZnO and ZnO@A-SWNT under 365 nm UV irradiation at an intensity of 0.47 mW cm^{-2} , with a bias of 2 V applied.

The voltage response fittings tend to have a smaller rise time pattern, where the rise time is shorter than the decay time. As presented in Table 3, the higher annealing temperature produces a smaller light state or rising time, and the dark time also shows a small value. Although the P-SWZ-175 has increased, it takes less than 1 second. Besides, the decay time pattern of the current and voltage photoresponse tends to be larger than the rise time pattern, as it is associated with the recombination charge delay event. When the solar simulator is turned on, electron-hole pairs are formed and recombined, while the trapped charges are suspended for recombination. Therefore,

Fig. 12 J - V curve of SWCNT and SWCNT/ZnO NCs integrated Si thin film.

it generates a longer photoresponse decay time until the trapped charge is released. Charge liberation occurs when the beam is re-ignited, and the charging occurs before the photo-induced carrier contributes/acts, showing a good response on the device.^{56,57}

SWCNT/ZnO NC-based solar cells, where the top layer had a more significant E_g than the below layer and was transparent to the light spectrum, allowing it to be easily transmitted and absorbed. The ZnO layer acts as an antireflection layer to enhance optical absorption and is a dopant carrier for series resistance reduction.¹⁴ Meanwhile, SWCNTs had high transparency and low resistivity. The high level of transparency in SWCNTs allows light to be absorbed easily. Besides, the use of Si can absorb most of the light coming from the SWCNT/ZnO NC layer, reducing energy loss during the energy conversion process. The performance test of the SWCNT/ZnO NC solar cell thin film was carried out under the light of a solar simulator with a power intensity of 100 mW cm^{-2} and an illuminated area of 2.2 cm^2 . The performance results of SWCNT/ZnO NCs on Si thin film are presented in the J - V curve in Fig. 12. The solar cell test under illumination consisted of several important parameters to determine the power conversion efficiency (PCE) of solar cells. The fill factor (FF) was calculated using the formula shown in eqn (3).⁴⁰

$$\text{FF} = \frac{V_m \times I_m}{V_{oc} \times I_{sc}} \quad (3)$$

Efficiency (η) is an important parameter representing the amount of light energy converted into electrical energy.

$$\eta = \frac{P_m}{P_{in}} = \frac{(\text{FF} \times I_{sc} \times V_{oc})}{P_{in}} \times 100\% \quad (4)$$

where P_m is the maximum output power and P_{in} is the incoming power.

SWCNT/ZnO NC-based Si solar cells with a combination of HCl and $\text{H}_2\text{SO}_4/\text{HNO}_3$ achieved an efficiency of 16.4% (Table 4). This chemical treatment of SWCNTs proved highly effective in boosting the performance of SWCNT-based solar cells. Shim *et al.*²⁴ reported an efficiency of 16.41% for SWCNT/Si solar cells with an active area of 3.25 cm^2 , attributing the improvement to the reduction of Fe impurities through chemical treatment. The addition of a ZnO layer to the SWCNT/ZnO NC films further enhanced solar cell performance, indicating an efficiency increase to 17.0%. Wang *et al.*³⁶ also observed an

efficiency gain in SWCNT/Si solar cells coated with ZnO layers, driven by higher short-circuit current (J_{sc}) and fill factor (FF).

Saidah *et al.*²³ demonstrated the SWCNT/ZnO without annealing treatment for SWCNT purification, achieving an efficiency of 8.71%.²³ Jia *et al.*⁵⁸ used NaCl for CNT treatment, obtaining an efficiency of 13.8%. In addition, an increase in SWCNT/ZnO NCs solar cell efficiency with different SWCNT annealing temperatures was observed. Samples P-SWZ-125, P-SWZ-150, and P-SWZ-175 showed an increase in efficiency of 17.5%, 18.1%, and 18.6%, respectively.

Annealing temperature treatment enhances cell performance. Our analysis indicates that higher efficiency is closely linked to improved test parameters. Specifically, the P-SWZ-100 sample exhibited increases in both J_{sc} and V_{oc} . The P-SWZ-125 sample experienced an increase in fill factor (FF), while the P-SWZ-150 sample showed an increase in J_{sc} . The rise in J_{sc} is attributed to enhanced light absorption, improved carrier separation at the interface, reduced light reflectance, and lower SWCNT series resistance.¹⁰ The overall increase in efficiency from $100 \text{ }^\circ\text{C}$ to $175 \text{ }^\circ\text{C}$ suggested that, as the annealing temperature rises, more charge carriers are able to overcome the activation energy barrier, facilitating greater electron movement.

4. Conclusion

For the first time, we observed that annealing treatment has a substantial impact on the SWCNT/ZnO NC integrated Si thin film. The XRD analysis revealed an increase in the intensity of the diffraction peak, indicating better crystallinity as the annealing temperature increased. In addition, the surface morphology of the film became more uniform with no agglomeration alongside the SWCNT fiber diameter decreasing while the percentage of film porosity increased with increasing temperature. The absorbance of SWCNT/ZnO NCs occurred in the UV light wavelength range of 246–326 nm. Higher annealing temperatures led to increased absorbance and a reduction in the bandgap (E_g). Moreover, the increased annealing temperature resulted in higher photocurrent, enabling a faster device response to light. Overall, the annealing treatment greatly impacted solar cell efficiency with efficiencies reaching up to 18.6% at an annealing temperature of $175 \text{ }^\circ\text{C}$. This efficiency gain was largely due to enhancements in crystallinity, porosity, absorbance, photocurrent, and a notable reduction in E_g .

Data availability

The author confirms that the data of this study are available within the article.

Author contributions

N. Mufti: supervision, validation, experimental setup, project administration. O. D. Ardilla and R. F. Wulandari: experimental, draft manuscript writing. E. S. Yuliana: manuscript

Table 4 Output performance parameter of SWCNT/ZnO NC-based solar cells

Parameters	I_{sc} (mA)	J_{sc} (mA cm^{-2})	V_{oc} (V)	FF	η (%)
Si	128	58.1	0.51	0.50	14.8
P-SW	187	85.2	0.49	0.39	16.4
P-SWZ-100	237	108	0.54	0.29	17.0
P-SWZ-125	225	102	0.53	0.32	17.5
P-SWZ-150	223	106	0.53	0.32	18.1
P-SWZ-175	239	109	0.52	0.33	18.6
Ref. 23	26.93	48.09	0.56	0.32	8.71
Ref. 58	—	36.3	0.53	0.72	13.8



writing, data analysis, data interpretation. A. Taufiq and H. Setiyanto: investigation, data validation, M. Aziz: supervision, reviewing, A. A. Salim: conceptualization, reviewing, editing, R. Suryana and W. Septina: discussion, interpretation.

Conflicts of interest

There are no conflicts to declare.

Acknowledgements

This research has received support funding from Universitas Negeri Malang through Indonesian Collaboration Research grant (RKI) no. 5.4.51/UN32.14.1/LT/2024. This manuscript is an honorable tribute to the lifelong achievements of T. T. M. Palstra.

References

- 1 S. R. Sharvini, Z. Z. Noor, C. S. Chong, L. C. Stringer and R. O. Yusuf, Energy consumption trends and their linkages with renewable energy policies in East and Southeast Asian countries: Challenges and opportunities, *Sustainable Environ. Res.*, 2018, **28**(6), 257–266.
- 2 D. G. Victor, F. W. Geels and N. Sharif, Accelerating the transition to sustainable energy, *Nat. Energy*, 2019, **4**(6), 451–459.
- 3 A. Moussa, H. Zidan and M. Aldarwish, Solar energy technologies: A review of their role in a sustainable energy system, *Renewable Sustainable Energy Rev.*, 2020, **119**, 109555.
- 4 S. Goktas and A. Goktas, A comparative study on recent progress in efficient ZnO based nanocomposite and heterojunction photocatalysts: A review, *J. Alloys Compd.*, 2021, **863**, 158734.
- 5 K. Znajdek, M. Sibiński, Z. Lisik, A. Apostoluk, Y. Zhu, B. Masenelli and P. Sędzicki, Zinc oxide nanoparticles for improvement of thin film photovoltaic structures' efficiency through down shifting conversion, *Opto-Electron. Rev.*, 2017, **25**(2), 99–102.
- 6 A. Goktas, F. Aslan, A. Tumbul and S. H. Gunduz, Tuning of structural, optical and dielectric constants by various transition metal doping in ZnO: TM (TM = Mn, Co, Fe) nanostructured thin films: a comparative study, *Ceram. Int.*, 2017, **43**(1), 704–713.
- 7 M. Lanjewar and J. V. Gohel, Enhanced performance of Ag-doped ZnO and pure ZnO thin films DSSCs prepared by sol-gel spin coating, *Inorg. Nano-Met. Chem.*, 2017, **47**(7), 1090–1096.
- 8 X. G. Hu, P. X. Hou, C. Liu, F. Zhang, G. Liu and H. M. Cheng, Small-bundle single-wall carbon nanotubes for high-efficiency silicon heterojunction solar cells, *Nano Energy*, 2018, **50**, 521–527.
- 9 M. Tomidokoro, S. Tunmee, U. Rittihong, C. Euaruksakul, R. Supruangnet, H. Nakajima and H. Akasaka, Electrical conduction properties of hydrogenated amorphous carbon films with different structures, *Materials*, 2021, **14**(9), 2355.
- 10 H. Sun, J. Wei, Y. Jia, X. Cui, K. Wang and D. Wu, Flexible carbon nanotube/mono-crystalline Si thin-film solar cells, *Nanoscale Res. Lett.*, 2014, **9**, 1–6.
- 11 J. Yan, C. Zhang, H. Li, X. Yang, L. Wan, F. Li and J. Chen, Stable organic passivated carbon nanotube–silicon solar cells with an efficiency of 22%, *Adv. Sci.*, 2021, **8**(20), 2102027.
- 12 M. A. Deshmukh, S. J. Park, B. S. Hedau and T. J. Ha, Recent progress in solar cells based on carbon nanomaterials, *Sol. Energy*, 2021, **220**, 953–990.
- 13 T. Zhang, S. Iqbal, X. Y. Zhang, W. Wu, D. Su and H. L. Zhou, Recent advances in highly efficient organic-silicon hybrid solar cells, *Sol. Energy Mater. Sol. Cells*, 2020, **204**, 110245.
- 14 F. Wang and K. Matsuda, In Applications of carbon nanotubes in solar cells, *Nanocarbons for energy conversion: supramolecular approaches*, Springer, Cham, 2019, pp. 497–536.
- 15 J. Ouyang, Applications of carbon nanotubes and graphene for third-generation solar cells and fuel cells, *Nano Mater. Sci.*, 2019, **1**(2), 77–90.
- 16 X. Hu, P. Hou, C. Liu and H. Cheng, Carbon nanotube/silicon heterojunctions for photovoltaic applications, *Nano Mater. Sci.*, 2019, **1**(3), 156–172.
- 17 J. Chen, D. D. Tune, K. Ge, H. Li and B. S. Flavel, Front and back-junction carbon nanotube-silicon solar cells with an industrial architecture, *Adv. Funct. Mater.*, 2020, **30**(17), 2000484.
- 18 X. Zhao, W. Xu, Y. Wu, H. Wu, Z. Xia, H. Xu and A. Cao, High-efficiency CNT-Si solar cells based on a collaborative system enabled by oxide penetration, *Nano Res.*, 2022, **15**(3), 2497–2504.
- 19 E. Aslan, G. Sahin and A. Goktas, Facile synthesis of Sb₂S₃ micro-materials for highly sensitive visible light photodetectors and photocatalytic applications, *Mater. Chem. Phys.*, 2023, **307**, 128160.
- 20 O. A. Gurova, V. E. Arhipov, V. O. Koroteev, T. Y. Guselnikova, I. P. Asanov, O. V. Sedelnikova and A. V. Okotrub, Purification of Single-Walled Carbon Nanotubes Using Acid Treatment and Magnetic Separation, *Phys. Status Solidi B*, 2019, **256**(9), 1800742.
- 21 S. Almalki, L. Yu, T. Grace, A. S. Bati and J. G. Shapter, Preparation of hybrid molybdenum disulfide/single wall carbon nanotube–n-type silicon solar cells, *Appl. Sci.*, 2019, **10**(1), 287.
- 22 L. Li, T. Zhai, Y. Bando and D. Golberg, Recent progress of one-dimensional ZnO nanostructured solar cells, *Nano Energy*, 2012, **1**(1), 91–106.
- 23 R. Saidah, N. Mufti, A. Taufiq and M. Diantoro, Improving the efficiency of solar cell based on ZnO/F-SWCNT/Si by functionalized SWCNTs as the photoactive layer, *AIP Conf. Proc.*, 2023, **2748**(1), 020051.
- 24 W. H. Shim, S. Y. Park, M. Y. Park, H. O. Seo, K. D. Kim, Y. D. Kim and D. C. Lim, Multifunctional SWCNT-ZnO



- nanocomposites for enhancing performance and stability of organic solar cells, *Adv. Mater.*, 2011, 23.
- 25 M. Lanjewar and J. V. Gohel, Enhanced performance of Ag-doped ZnO and pure ZnO thin films DSSCs prepared by sol-gel spin coating, *Inorg. Nano-Met. Chem.*, 2017, 47(7), 1090–1096.
 - 26 S. Goktas and A. Goktas, A comparative study on recent progress in efficient ZnO based nanocomposite and hetero-junction photocatalysts: A review, *J. Alloys Compd.*, 2021, 863, 158734.
 - 27 F. Aslan, G. Adam, P. Stadler, A. Goktas, I. H. Mutlu and N. S. Sariciftci, Sol-gel derived In₂S₃ buffer layers for inverted organic photovoltaic cells, *Sol. Energy*, 2014, 108, 230–237.
 - 28 K. Domagała, M. Borlaf, J. Traber, D. Kata and T. Graule, Purification and functionalisation of multi-walled carbon nanotubes, *Mater. Lett.*, 2019, 253, 272–275.
 - 29 M. N. Durso and A. J. Hart, Purification of dense carbon nanotube networks by subcritical hydrothermal processing, *Carbon Trends*, 2022, 9, 100206.
 - 30 Y. R. Park, N. Liu and C. J. Lee, Photoluminescence enhancement from hybrid structures of metallic single-walled carbon nanotube/ZnO films, *Curr. Appl. Phys.*, 2013, 13(9), 2026–2032.
 - 31 D. D. Thongam and H. Chaturvedi, Functionalization of pristine, metallic, and semiconducting-SWCNTs by ZnO for efficient charge carrier transfer: analysis through critical coagulation concentration, *ACS Omega*, 2022, 7(17), 14784–14796.
 - 32 A. Goktas, A. Tumbul, Z. Aba and M. J. T. S. F. Durgun, Mg doping levels and annealing temperature induced structural, optical and electrical properties of highly c-axis oriented ZnO: Mg thin films and Al/ZnO: Mg/p-Si/Al hetero-junction diode, *Thin Solid Films*, 2019, 680, 20–30.
 - 33 A. Wibowo, M. A. Marsudi, M. I. Amal, M. B. Ananda, R. Stephanie, H. Ardy and L. J. Diguna, ZnO nanostructured materials for emerging solar cell applications, *RSC Adv.*, 2020, 10(70), 42838–42859.
 - 34 A. Goktas, F. Aslan, A. Tumbul and S. H. Gunduz, Tuning of structural, optical and dielectric constants by various transition metal doping in ZnO: TM (TM= Mn, Co, Fe) nanostructured thin films: a comparative study, *Ceram. Int.*, 2017, 43(1), 704–713.
 - 35 T. H. Flemban, M. A. Haque, I. Ajia, N. Alwadai, S. Mitra, T. Wu and I. S. Roqan, A photodetector based on p-Si/n-ZnO nanotube heterojunctions with high ultraviolet responsivity, *ACS Appl. Mater. Interfaces*, 2017, 9(42), 37120–37127.
 - 36 F. Wang, D. Kozawa, Y. Miyauchi, K. Hiraoka, S. Mouri, Y. Ohno and K. Matsuda, Considerably improved photovoltaic performance of carbon nanotube-based solar cells using metal oxide layers, *Nat. Commun.*, 2015, 6(1), 6305.
 - 37 Z. Aba, A. Goktas and A. Kilic, Characterization of Zn_{1-x}LaxS thin films; compositional, surface, optical, and photoluminescence properties for possible optoelectronic and photocatalytic applications, *J. Sol-Gel Sci. Technol.*, 2024, 109(1), 260–271.
 - 38 L. T. M. Hoa, Characterization of multi-walled carbon nanotubes functionalized by a mixture of HNO₃/H₂SO₄, *Diam. Relat. Mater.*, 2018, 89, 43–51.
 - 39 K. P. Sapkota, I. Lee, M. A. Hanif, M. A. Islam and J. R. Hahn, Solar-light-driven efficient ZnO–single-walled carbon nanotube photocatalyst for the degradation of a persistent water pollutant organic dye, *Catalysts*, 2019, 9(6), 498.
 - 40 Z. S. Sadeq, S. M. Alshrefi, W. R. Saleh and D. K. Mahdi, IV characteristics of n-Si/ZnO/Se/MWCNTs nanocomposite solar cell fabricated by solvothermal technique, *AIP Conf. Proc.*, 2019, 2190(1), 020085.
 - 41 E. Shi, L. Zhang, Z. Li, P. Li, Y. Shang, Y. Jia and A. Cao, TiO₂-coated carbon nanotube-silicon solar cells with efficiency of 15%, *Sci. Rep.*, 2012, 2(1), 884.
 - 42 M. S. P. Sarah, F. S. S. Zahid and M. Rusop, Investigation on IV for Different Heating Temperatures of Nanocomposited MEH-PPV: CNTs Organic Solar Cells, *Int. J. Photoenergy*, 2012, 2012(1), 872324.
 - 43 R. Shafique, H. Latif, A. Sattar and S. A. Shabbir, Effect of anti-reflecting layers on device performance of SWCNTs/Si hetero-junction hybrid solar cells, *Opt. Mater.*, 2023, 143, 114215.
 - 44 M. S. Choi, T. Park, W. J. Kim and J. Hur, High-performance ultraviolet photodetector based on a zinc oxide nanoparticle@ single-walled carbon nanotube heterojunction hybrid film, *Nanomaterials*, 2020, 10(2), 395.
 - 45 A. Mahesh, I. N. Jawahar and V. Biju, Photogenerated charge carrier processes in carbonate derived nanocrystalline ZnO: photoluminescence, photocurrent response and photocatalytic activity, *Appl. Phys. A: Mater. Sci. Process.*, 2024, 130(5), 360.
 - 46 T. Y. Yousif and A. N. Naje, Characterization of carbon nanotube decorated silver nanoparticles, *J. Phys.: Conf. Ser.*, 2021, 1879(3), 032093.
 - 47 S. Zuo, X. Li, W. Liu, Y. He, Z. Xiao and C. Zhu, Field emission properties of the dendritic carbon nanotubes film embedded with ZnO quantum dots, *J. Nanomater.*, 2011, 2011(1), 382068.
 - 48 N. Tripathi, V. Pavelyev and S. S. Islam, Tunable growth of single-wall CNTs by monitoring temperature increasing rate, *Int. Nano Lett.*, 2018, 8, 101–109.
 - 49 P. E. Georghiou, G. Valluru, C. Schneider, S. Liang, K. Woolridge, K. Mulla and Y. Zhao, Dispersion of single-walled carbon nanotubes into aqueous solutions using Poh's cyclotetrachromo-tropylene (CTCT), *RSC Adv.*, 2014, 4(60), 31614–31617.
 - 50 K. Nagpal, L. Rapenne, D. S. Wragg, E. Rauwel and P. Rauwel, The role of CNT in surface defect passivation and UV emission intensification of ZnO nanoparticles, *Nanomater. Nanotechnol.*, 2022, 12, 18479804221079419.
 - 51 M. Kurban, Electronic structure, optical and structural properties of Si, Ni, B and N-doped a carbon nanotube: DFT study, *Optik*, 2018, 172, 295–301.
 - 52 Y. Ziat, M. Hammi, H. Belkhanchi, O. Ifiguis, S. Rzaoudi, C. Laghlimi and C. Lazrak, CNTs modified ZnO and TiO₂ thin films: The effect of loading rate on band offset at metal/semiconductor interfaces, *E3S Web Conf.*, 2022, 337, 05003.



- 53 A. Doyan, S. Susilawati and M. Taufik, The Effect of Temperature Variations on the Optical Properties of Tin Oxide Film with Doping Aluminum, Fluorine and Indium for Semiconductor Electronic Devices, *Mater. Sci. Forum*, 2021, **1028**, 77–83.
- 54 L. Chu, R. Hu, W. Liu, Y. Ma, R. Zhang, J. Yang and X. A. Li, Screen printing large area organometal halide perovskite thin films for efficient photodetectors, *Mater. Res. Bull.*, 2018, **98**, 322–327.
- 55 B. D. Boruah, Zinc oxide ultraviolet photodetectors: rapid progress from conventional to self-powered photodetectors, *Nanoscale Adv.*, 2019, **1**(6), 2059–2085.
- 56 T. S. Walmsley, B. Chamlagain, U. Rijal, T. Wang, Z. Zhou and Y. Q. Xu, Gate-Tunable Photoresponse Time in Black Phosphorus–MoS₂ Heterojunctions, *Adv. Opt. Mater.*, 2019, **7**(5), 1800832.
- 57 B. Cao, X. Shen, J. Shang, C. Cong, W. Yang, M. Eginligil and T. Yu, Low temperature photoresponse of monolayer tungsten disulphide, *APL Mater.*, 2014, **2**, 11.
- 58 Y. Jia, A. Cao, X. Bai, Z. Li, L. Zhang, N. Guo and P. M. Ajayan, Achieving high efficiency silicon-carbon nanotube heterojunction solar cells by acid doping, *Nano Lett.*, 2011, **11**(5), 1901–1905.

